PCCP

Rotational quenching of an interstellar gas thermometer: CH$_3$CN...He collisions.

Journal Name

ARTICLE TYPE

Rotational quenching of an interstellar gas thermometer: CH$_3$CN···He collisions.

M. Ben Khalifa,[*a,b] E. Quintas-Sánchez,[c] R. Dawes,[c] K. Hammami,[b] and L. Wiesenfeld[†a]

Among all the molecular species found in the interstellar medium, molecules with three-fold symmetry axes play a special role, as their rotational spectroscopy allows them to act as practical gas thermometers. Methyl-cyanide (CH$_3$CN) is the second most abundant of those (after ammonia). We compute in this paper the collisional dynamics of methyl-cyanide in collision with helium, for both the *A*- and the *E*- symmetries of CH$_3$CN. The potential energy surface is determined using the CCSD(T)-F12*b* formalism and fit with convenient analytic functions. We compute the rotationally inelastic cross sections for all levels up to 510 cm^{-1} of collision energy, employing at low energy exact Coupled Channels methods, and at higher energies, approximate Coupled States methods. For temperatures from 7 K up to 300 K, rates of quenching are computed and most are found to differ from those reported earlier (up to a factor of a thousand), calling for a possible reexamination of the temperatures assigned to low density gasses.

1 Introduction

So far, more than 190 molecules of different classes have been detected in molecular clouds, and among them, at least 50 molecules with a C≡N nitrile (or cyano) function.[1] Among those, CH$_3$CN is of particular interest. Methyl-cyanide, also called cyanomethane or acetonitrile, is an inert trace gas in Earth's atmosphere with a lifetime of many months. CH$_3$CN is among the earliest molecules to have been identified in the InterStellar Material (ISM) environment,[2] thanks to its numerous observable transitions in the 110 GHz region. It was detected towards the massive star-forming regions Sagittarius A and B, close to the Galactic center.[3] Since then, CH$_3$CN was also identified ubiquitously, *e.g.* in the TMC-1 dark clouds,[4] the low-mass protostar IRAS 16293-2422,[5] in the circumstellar shell of the carbon-rich star IRC +10216,[6] in comets, such as Kohoutek.[7] Recently, large quantities of CH$_3$CN in the protoplanetary disk surrounding the young star MWC-480 were

detected thanks to the ALMA observatory.[8]

The strong electric dipole moment ($\mu = 3.913$ Debye)[9], its favorable partition function, and its relative chemical abundance make it one of the easiest organic molecule to detect. Its particular rotational spectroscopy (because of its C_{3v} symmetry) and its very prolate character make it an ideal probe for the characterization of the physical conditions of the gas observed. CH$_3$CN shares these peculiarities with another, in this sense very similar molecule, propyne (CH$_3$CCH), even if their chemical backgrounds are different.

For prolate C_{3v} type of molecules, transitions having the same value of J with different K (where J is the total angular momentum quantum number of CH$_3$CN, and K is the projection of J on the C_3 rotational axis), have practically the same transition frequencies (see Pols *et al.*[3] for a vivid example). Thus, transitions which arise from different rotational energy levels occur in fairly narrow frequency regions, and many transitions can be identified simultaneously using the same antenna settings and sensitivities. This can helps to reduce the impact of calibration errors. The radiative transition between different values of K-ladders are forbidden by the radiative selection rule ($\Delta J = \pm 1$, $\Delta K = 0$). The relative intensity of transitions

a Laboratoire Aimé-Cotton, CNRS and Université Paris-Saclay, Orsay, France. laurent.wiesenfeld@u-psud.fr

b Laboratoire de Spectroscopie Atomique Moléculaire et Applications, Université Tunis El-Manar, Tunis, Tunisie. malek.benkhalifa@fst.utm.tn

c Missouri University of Science and Technology, Rolla, MO 65409-0010, USA

of the type $J_K \rightarrow (J-1)_K$ for different K-components will to first order be determined by the gas kinetic temperature of the colliding particles. Nevertheless, the population exchange between the different ladders of K is fundamentally carried out via collisional processes, and for that reason, the relative populations of these levels are related to the kinetic temperature of the medium by the equilibrium statistical equations. Hence, thanks to these spectroscopic properties, CH_3CN may act as an effective thermometer of the ISM.

In this paper, we aim to study the rotational (de)-excitation of CH_3CN colliding with He using a new potential energy surface (PES). Similar computations were carried out by Green in 1985.[10] We will provide a precise set of quenching rate for the CH_3CN-He collisional system.

The paper is organized as follows. The potential energy surface describing the $CH_3CN\cdots He$ interaction is presented in section 2. In section 3 we describe the scattering calculations, including cross sections and quenching rates. A comparison of the present results with the previous ones of Green is given in section 4.

2 Potential energy surface

2.1 Ab initio points

The coordinates used to define the three-dimensional (3D) intermolecular CH_3CN–He interaction: R, θ, and ϕ, are depicted in Fig. 1. The frame of reference is fixed to the CH_3CN molecule in such a way that its origin is at the center-of-mass, its z axis is along the symmetry axis, and its zx plane contains one of the hydrogen atoms. R represents the distance between the center-of-mass of the CH_3CN molecule and the helium atom, while θ and ϕ represent the spherical angles. The geometry of the CH_3CN molecule was held rigid, using experimentally-determined parameters reported previously:[11] $r(N–C)= 1.156$ Å, $r(C–C)= 1.457$ Å, $r(C–H)= 1.087$ Å, and $\angle(HCC)= 110.1°$. Masses of 14.0030740048, 1.007825032, 12 and 4.00260325413 amu were used for ^{14}N, ^{1}H, ^{12}C and ^{4}He, respectively. The non-bonded interaction energies were computed using explicitly-correlated coupled-cluster theory[12] extended to the complete basis set limit (CCSD(T)-F12b/CBS). The basis extrapolation was performed using the Peterson VTZ-F12 and VQZ-F12 bases[13] and the l^{-3} formula. The triples contributions, (T), from each basis set, were not separately scaled (e.g., based on MP2-F12/MP2 energies), but rather were included in the extrapolation of total energies. The helium atom presents a slight complication since corresponding default auxiliary basis sets—needed for the F12 calculations—have not yet been published. Moreover, in the case of He-atom–molecule interactions, small numerical discrepancies in the long range region of the PES
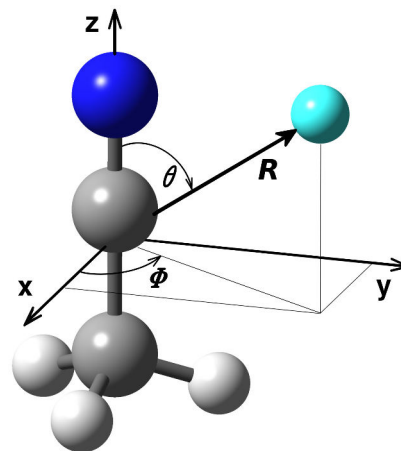

Fig. 1 Coordinates used to describe the $CH_3CN\cdots He$ interaction. R: center-of-mass separation, θ and ϕ: spherical angles. The origin of the frame of reference is at the center-of-mass of the CH_3CN molecule.

(possibly attributable to the auxiliary basis) have been reported previously by others[14] and also found in our experience.[15] Therefore we employed large auxiliary bases and performed several test cuts in order to confirm good convergence as well as physically sensible behavior. The augmented correlation-consistent valence quintuple-ζ basis from second-order Møller-Plesset perturbation theory (av5z/mp2fit)[16] and the segmented contracted highly polarized quadruple-ζ valence quality (def2-qzvpp/jkfit)[17] basis sets were specified for the density fitting (DF) and resolution of the identity (RI) bases, respectively. No convergence issues or irregularities were detected within the fitted range of 1.7 Å$< R < 15.0$ Å, and we did not observe any lack of size consistency (the PES was computed as a supersystem in any case). All *ab initio* calculations were performed using the Molpro electronic structure code package.[18]

In contrast to earlier work, where the PES was constructed from a very large number of ab initio points,[19,20] this 3D PES was constructed using an automated interpolating moving least squares methodology, which has been used in several previous studies[21–25] and has been recently released as a software package under the name AUTOSURF.[26] This interpolative approach can accommodate arbitrary energy-surface topographies and is particularly advantageous in cases with large anisotropy, which are challenging for traditional quadrature-type expansions. The shortest inter-monomer center-of-mass distance considered is $R = 1.7$ Å, with the additional restriction of a maximum repulsive energy of 6 kcal/mol (~ 2100 cm^{-1}) above the separated monomers asymptote. Taking advantage of the C_{3v} symmetry of the system, energies are only
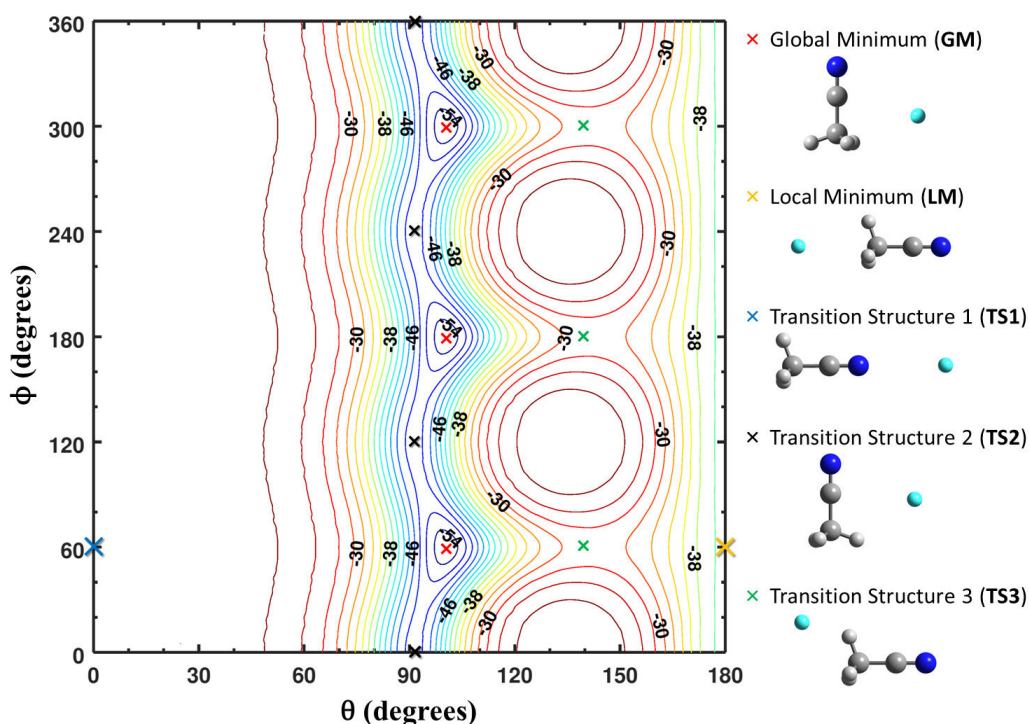
Fig. 2 R-optimized contour plot of the PES as a function of the spherical angles θ and ϕ. For each pair of angles, the energy (given in cm^{-1}) is optimized with respect to the center-of-mass distance R. The position of stationary points—and the corresponding molecular configuration—is also highlighted. See the text for details.

computed in the reduced angular range: $0 < \phi < 60°$. To guide the placement of high-level data—and avoid computing and discarding computationally expensive *ab initio* energies in highly repulsive regions—an initial lower-level guide surface (at the MP2/AVDZ level of theory) was constructed using a set of 3431 symmetry-unique points, distributed using a Sobol sequence biased to sample the short range region more densely. For the high-level PES, the final global root-mean-squared fitting error was 0.05 cm^{-1} for energy-regions below the asymptote, and the total number of automatically generated symmetry-unique points needed to reach that target was 2176. As usual,[27] a local fit was expanded about each data point (using, for this particular system, a fitting basis composed of 109 functions) and the final potential is obtained as the normalized weighted sum of the local fits. The analytical representation of the PES is available from the authors upon request.

Fig. 2 shows a 2D representation of the PES (denoted R-optimized) as a function of the spherical angles θ and ϕ (as defined in Fig. 1). For each pair of angles, the energy is relaxed (minimized) with respect to the center-of-mass distance R. This type of plot provides unique insight into the isomers in the system, since it includes all minima and the barriers between them. The position of stationary points and the corresponding molecular configurations of the sys-

tem are also highlighted in the figure. The z axis is the symmetry axis of the CH$_3$CN molecule, such that $\theta = 0°$, places the He-atom directly above the N-atom. $\phi = 0°$, places the He atom in the same plane as the z axis and one of the C–H bonds. As can be seen in the figure, the PES has perfect 3-fold symmetry as well as vertical mirror planes each $\Delta\phi = 120°$. The global minimum has a well depth of 55.16 cm^{-1}; its periodicity and locations—between H-atoms, nearly equatorial—is clear. A second (local) minimum exists at $\theta = 180°$, with a well depth of 40.45 cm^{-1}. The PES is not dependent on the value of ϕ (which is undefined) at $\theta = 180°$; but when $\theta = 180° - \varepsilon$ (with ε being a small angle) the shape of the molecule (and the value of the potential energy) is almost the same for any value of ϕ and therefore the label for the local minimum could be put anywhere along the ϕ axis. The same is true for the transition structure 1, located at $\theta = 0°$. We choose to place both labels at $\phi = 60°$, in Fig. 2. The energies—relative to the asymptote: $V(R \to \infty)$—and the geometric parameters of the minima and transition structures highlighted in the figure, are given in Table 1.

Fig. 3 shows the potential as a function of R upon approach toward each of the stationary points highlighted in Fig. 2. The variation in those cuts gives some indication of the anisotropy of the interactions. The strength
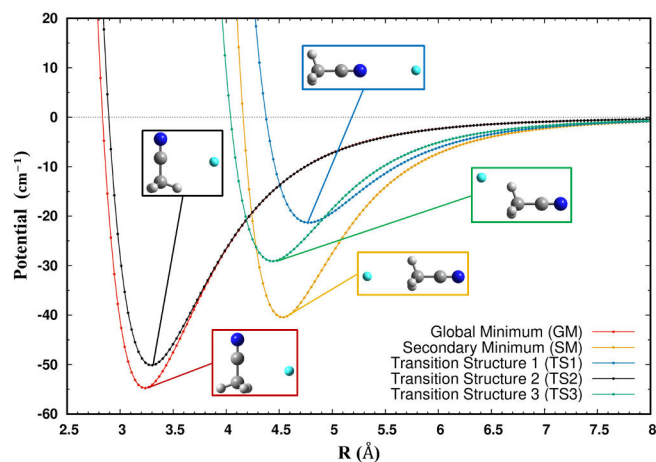
Fig. 3 Radial cuts through the PES are shown for approach towards each of the stationary points highlighted in Fig. 2, along their respective angular coordinates (given in Table 1).

and anisotropy of the PES describing the interaction between collision partners govern the scattering dynamics and, hence, the derived cross sections, propensities, and rate coefficients. In order to better appreciate the topography of the PES near the global minimum, additional 2D plots of the potential are shown in Fig. 4. The plots explore the region around the global minimum, by presenting both the (R, ϕ) and (R, θ) planes that cross it.

2.2 Analytical Representation

For the scattering calculations, it is convenient to fit the 3D-PES to an analytical representation. Such a procedure leads us to generate the $V(R, \theta, \phi)$ numerical expansion, which is implemented in the dynamical calculations. At each distance R, the *ab-initio* values of V were fitted by a weighted least square method to a spherical expansion,

$$V(R, \theta, \phi) = \sum_{\lambda=0}^{\lambda_{max}} \sum_{\mu=0}^{\lambda} V_{\lambda\mu}(R) Y_{\lambda}^{\mu}(\theta, \phi) \qquad (1)$$

	GM	LM	TS1	TS2	TS3
R	3.250	4.532	4.779	3.304	4.445
θ	100.4	180.0	0.0	91.3	141.7
ϕ	60.0	—	—	0.0	60.0
V	-55.16	-40.45	-21.32	-50.79	-29.10

Table 1 Geometric parameters and potential energy for the global (GM) and local (LM) minimum, as well as the transition structures (TS) of the CH_3CN–He complex—as defined in Fig. 2. All energies are given relative to the asymptote. Distances are in Angströms, angles are in degrees, and energies are in cm^{-1}. For LM and TS1, ϕ is undefined.
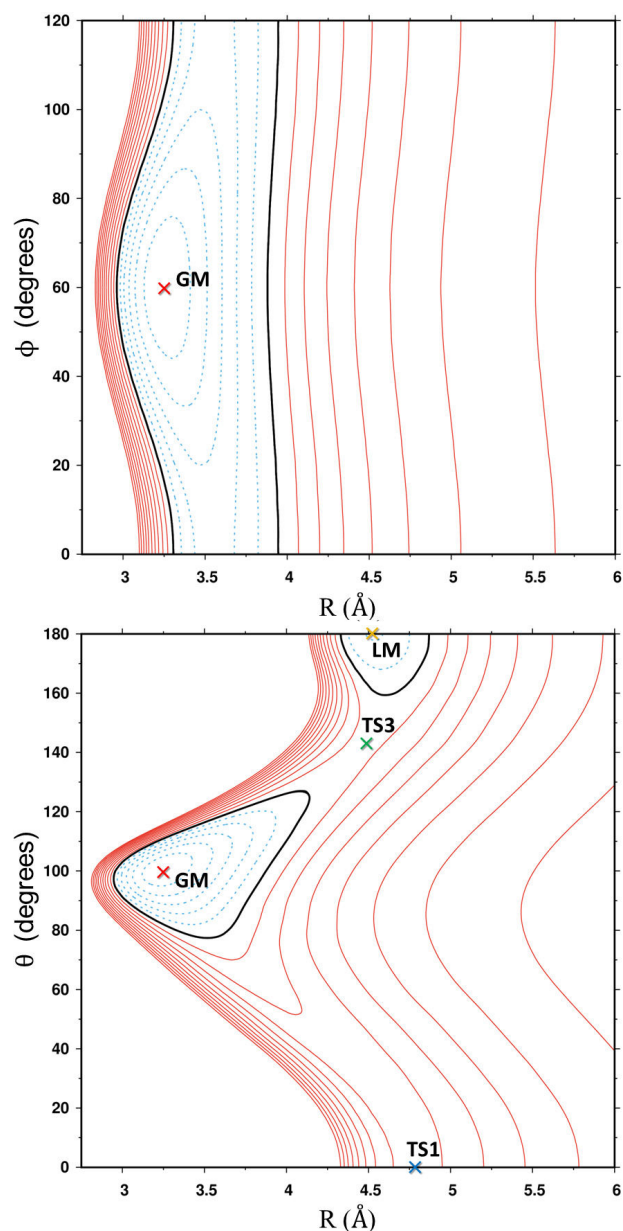

Fig. 4 2D cuts of the PES exploring the region around the global minimum, holding the angle θ (top panel) and ϕ (bottom panel) fixed at $100.4°$, and $60.0°$, respectively. The black contour represents the energy $E_0 = -32 \, cm^{-1}$. Dashed (solid) contours represents energies below (above) E_0, in steps of $4 \, cm^{-1}$. The position of stationary points—defined in Fig. 2—is also highlighted.

The interaction potential is real and symmetric with respect to reflexion in the (xz) plane which implies:

$$V(\lambda, -\mu)(R) = (-1)^{\mu} V_{\lambda\mu}(R)^* \qquad (2)$$

Using the property of the spherical harmonics, the interaction potential can then be written as:

$$V(R, \theta, \phi) = \sum_{\lambda=0}^{\lambda_{max}} \sum_{\mu=0}^{\lambda} V_{\lambda\mu}(R) \frac{Y_{\lambda}^{\mu}(\theta, \phi) + (-1)^{\mu} Y_{\lambda}^{-\mu}(\theta, \phi)}{1 + \delta_{\mu,0}} \qquad (3)$$

where $Y_{\lambda}^{\mu}(\theta, \phi)$ denotes the spherical harmonic, $V_{\lambda,\mu}(R)$ are the radial coefficients to be calculated and $\delta_{\mu,0}$ is is the Kronecker symbol.

In this case, the C_{3v} symmetry of the CH_3CN molecule constrains further the parity of the expansion. Indeed, only those coefficients with $\mu = 3n$ (n integer) are non-zero. From a PES grid containing (19×7) values of (θ, ϕ), we were able to include terms up to $\lambda_{max} = 18$ and $\mu_{max} = 6$. The number of fitting functions was limited to 70, with a precision in fitting the interpolated *ab-initio* PES data points of better than 1%. A slightly larger error is found for the smallest values of R.

Since it is crucial for the dynamical computations to have continuous angular coefficients, the analytic form of the interaction energy was obtained by an exponential extrapolation of $V_{\lambda\mu}(R)$ at the short distances ($R \leq 2$ bohr) and inverse exponent expansion at large distances ($R \geq 20$ bohr) using the POTENL routine of the Molscat code.[28]

3 Scattering calculations

In this section, we focus on the quantum dynamical treatment of the symmetric top molecule CH_3CN, impacted by He, in order to determine a pragmatic way to perform detailed scattering calculations in the close-coupling and/or coupled-states formalisms, at lower and higher energies, respectively. We aim for relevant accuracy for astrophysical applications, within a reasonable computational cost.

3.1 Spectroscopy

In order to compute the state-to-state inelastic cross sections, the spectroscopy of CH_3CN must be accurately reproduced by the code. CH_3CN is a prolate symmetric top, with the rotational constant for rotation along Oz being much larger than the two other rotation constants, which are equal. The energy levels for the symmetric top rotor are given by, at fourth order:

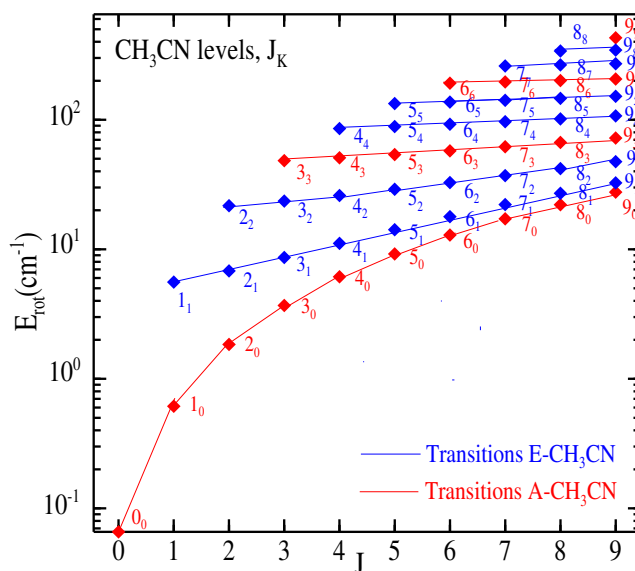$$E_{J,K} = BJ(J+1) + (C-B)K^2 + D_J J^2 (J+1)^2 - D_{JK} J(J+1) K^2$$
$$- D_K K^4 \qquad (4)$$

Fig. 5 Rotational levels of A-CH_3CN (red lines) and E-CH_3CN (blue lines) with energies less than 300 cm^{-1}. Optically allowed transitions (blue and red thin lines) connect levels with the same $K' = K$, and $J' = J \pm 1$

with (in cm^{-1}): $A = B = 0.3068$ and $C = 5.2470$,[10] and the centrifugal distortion constants: $D_J = 1.27E-07$, $D_K = 5.90E-06$, and $D_{JK} = 9.44E-05$.[29] Because of the identity of the hydrogen atoms and their nuclear spin $I = 1/2$, CH_3CN is split into two nuclear spin species (A- and E-CH_3CN), in a similar way to the *para* and *ortho* states of H_2 or H_2O. Rotational levels associated to A-CH_3CN have $K = 3n$, including also $K = 0$, and levels with $K = 3n \pm 1$ are associated to the E-CH_3CN. The spectrum of A- and E-CH_3CN rotational levels is depicted in Fig. 5. It shows that the rotational levels are very close to one another, because of the slow increase in energy with varying J, all the more with increasing K.

It must be stressed that because the PES reflects the overall symmetry of the problem, and hence, possesses the C_{3v} symmetry (see the restriction of $\mu = 3n$, equation 1), A- and E- levels are disconnected not only spectroscopically but also collisionally: If the rigid rotor approximation is valid, collisional excitation or quenching *does not* connect the A- and E- levels, confirming the quasi-independence of A- and E- level dynamics.

However, observationally, it is customary to record all possible transitions in one frequency range, being it between A- or E- levels. A typical case is given by Table 1 of Pols *et al.*[3] They observed as many transitions as possible in the 220 to 257 GHz range (12_K to 11_K, $K = 0, \ldots, 6$; 13_K

to 12_K and 14_K to 13_K, both with $K = 0,\ldots,9$), thereby covering a large range in energy (see Fig. 5) and a small range in frequencies. Many similar ranges may be found in the large number of observational papers.

Hence, even with the division into A- and E-CH$_3$CN symmetry species, the number of relevant levels is large and covers roughly $J \le 15$, $K \le 14$. For temperatures up to 300 K, many levels must be included in the dynamical computations. Using the Close-Coupling (CC) method[30] would be very expensive in computational time, especially so for collisions involving higher J_K levels. Accordingly, we used both the CC exact formalism and the Coupled-State (CS) approximation[31] in order to compute cross sections involving all rotational levels. Details are explained in the next section.

3.2 Cross-section calculation

All scattering computations were performed with the Molscat code,[28] suitably modified for use on parallel machines and with large representative matrices.

For astrophysical purposes, we converge our scattering calculations up to $J_K = 18_9$ for A-CH$_3$CN ($E_{rot} \le 506.45$ cm^{-1}) and $J_K = 18_8$ for E-CH$_3$CN ($E_{rot} \le 422.28$ cm^{-1}). Because our computations need a large rotational basis set for CH$_3$CN in order to converge, the full CC calculation proves to be very expensive. To keep computational times under control, the state-to-state cross sections $\sigma(E_{total})_{J'K'\leftarrow JK}$ were computed using the CC method for $E_{total} \le 100$ cm^{-1}, and the CS approximation for higher energies, up to $E_{total} \sim 1500$ cm^{-1}. Vibrational modes of the CH$_3$CN molecules could be causes of concern. The CCN bending mode is $\nu_{CCN} = 365$ cm^{-1} and the C-C stretching mode is $\nu_{CC} = 920$ cm^{-1}. We neglected the (de-)excitation of those bending and stretching modes. Previous work[32–34] showed that the rotational transitions cross sections and rates are much smaller in magnitude, especially so for energies not too far from the vibrational threshold. It is certain this approximation becomes poorer for higher temperatures, when the vibrational levels become significantly populated,[35].

The reduced mass is taken as $\mu = 3.646$ atomic mass units (isotopes ^{1}H,^{4}He,^{12}C and ^{14}N). As the A- and E- levels of CH$_3$CN must not interchange in inelastic collisions, cross sections have been treated separately for each nuclear spin species.

Fig. 6 highlights the low-energy quantum scattering at energies $E_c \le 100$ cm^{-1} for transitions to the ground state, while Fig. 7 represents the kinetic energy dependence of quenching cross sections for optically allowed transitions. We note that all the cross-sections have the same typical low energy shapes. Some weak resonances are present in the low energy region. Cross sections become smooth and less visible for larger values of ΔJ and decrease exponentially for $E_c \gtrsim 50$ cm^{-1} .

The rotational basis set for the quantum scattering computations was chosen as follows. For A-CH$_3$CN$-$He, rotational basis set is taken as $J \le 20$, $K = 0, 3$ for $E_{total} \le 50$ cm^{-1}; $J \le 20$, $K \le 9$ for $50 < E_{total} \le 100$ cm^{-1}; and $J \le 34$, $K \le 15$ for $E_{total} > 100$ cm^{-1}. For E-CH$_3$CN$-$He, we take $J \le 21$, $K \le 7$ for $E_{total} \le 100$ cm^{-1}; and $J \le 32$, $K = 16$ for $E_{total} > 100$ cm^{-1}. All the other parameters of the Molscat code were kept standard.

We estimate the convergence of the cross section to be of the order of 20–30 %, even if this is difficult to evaluate. We have also carefully described the cross sections above the different rotational thresholds (energy steps were taken small enough), in order to correctly describe the resonance structures of the cross sections, and not to bias the subsequent rates calculation.

Examples of quenching cross sections associated to A- and E-CH$_3$CN colliding with He are illustrated in Figs. 6 and 7.

3.3 Rate Coefficients

In order to accurately estimate the abundance of CH$_3$CN in the interstellar medium, we calculated quenching rate coefficients between two rotational levels: $J'_{K'} \leftarrow J_K$. The relevant state-to-state cross section ($\sigma_{J'K'\leftarrow JK}$) is integrated over a Maxwell Boltzmann velocity distribution $f(E_c)$. The rate is defined as:

$$k_{f\leftarrow i}(T) = \int_0^\infty \sigma_{f\leftarrow i}(E_c)f(E_c)dE_c \qquad (5)$$

with a normalized density probability,

$$f(E_c) = \left(\frac{8}{\pi\mu k_B^3 T^3}\right)^{\frac{1}{2}} E_c \exp\left(-\frac{E_c}{k_B T}\right) \qquad (6)$$

where E_c represents the collision energy, μ is the reduced mass, k_B and T denote the Boltzmann constant and the kinetic temperature, respectively. Examples of quenching rate coefficients are shown in Figs. 8 and 9.

Our calculations were performed for total energies ranging between 1 and 1500 cm^{-1}, in order to converge collision rate coefficients of the first 200 rotational levels for $7 \le T \le 300$ K. We note that for $T = 300$ K, the highest temperature considered in this work, we had to compute rotational cross sections up to $E_c = 1000$ cm^{-1}, that is, about $E_{tot} = 1500$ cm^{-1}, for both A- and E-CH$_3$CN. Hence, for higher energies, we had to finalize our calculation with computing only the $J_{tot} = 0, 2, \ldots$ partial waves, in order to
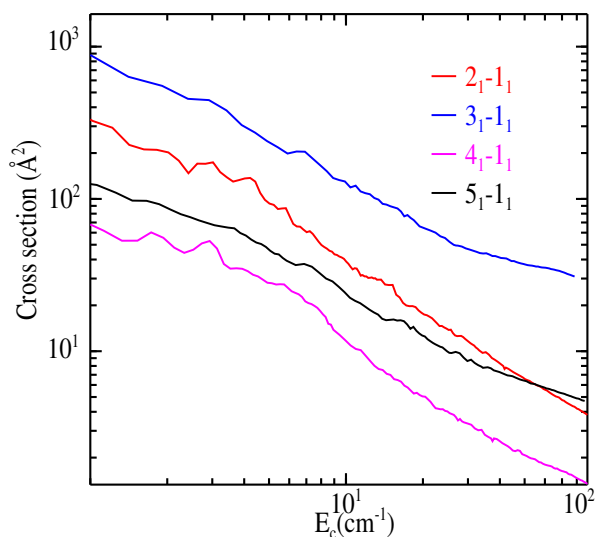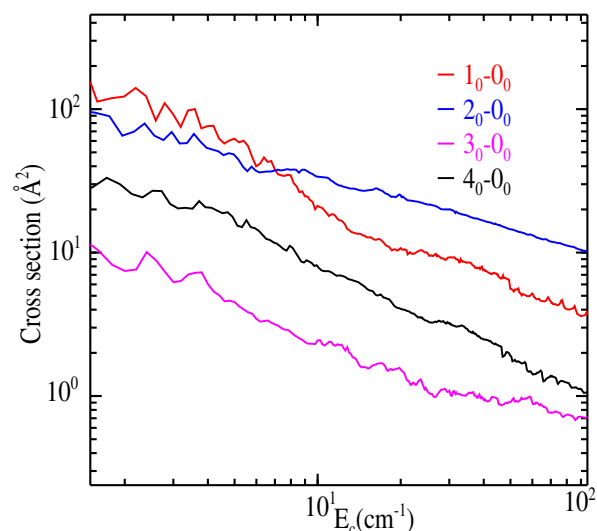
Fig. 7 Cross sections for rotational de-excitation, both *A*- and *E*-CH$_3$CN, for optically allowed transitions in the 220 GHz band.

Fig. 6 Cross section for the de-excitation of *A*- (top panel) and *E*- (bottom panel) CH$_3$CN as a function of the collisional energy E_c. Quenching towards ground state, respectively 0_0 and 1_1.
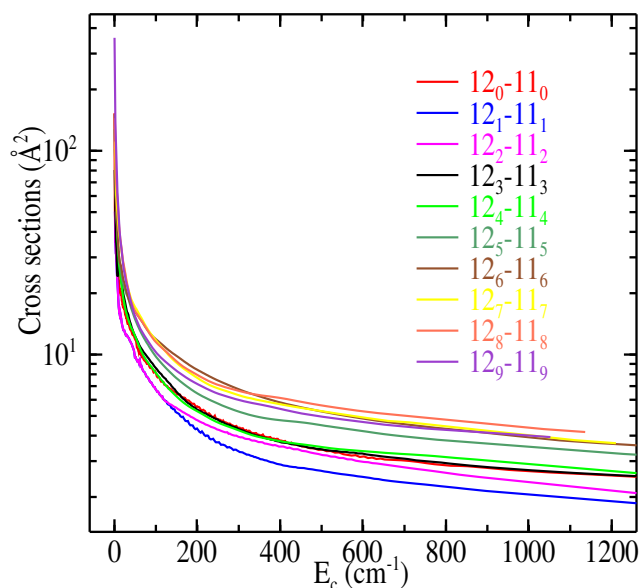
lessen calculation time. Benchmarking showed a decrease in the accuracy of calculations in cross section resulting in 25–30% in the rates, for the higher upper levels.

4 Discussion-Conclusion

The PES describing the CH$_3$CN···He interaction shows a shallow minimum (all energies in cm^{-1}) at $E_{GM} = -55.45$, comparable to similar cases, like H$_2$CO···He, $E_{GM} = -59.5$,[36] or $l-$C$_3$H$_2$···He, $E_{GM} = -56.00$.[20] On the contrary, much deeper wells for collisions of dipole-bearing molecules with H$_2$ are observed, like H$_2$CO···H$_2$:[37] Minimum at -312 (at -131, if averaged over H$_2$ orientation) because of both the large anisotropic polarizability and quadrupole moment of H$_2$.

The potential displays a rich structure, with a clear 3-fold symmetry, but also not so large a difference between the two ends, with E_{LM} ($\theta = 180°$, methyl end) not so different from E_{TS1}, ($\theta = 0°$, cyano end), see Table 1 and Fig. 4.

This shallow well, and possibly also the complex structure of the potential, is reflected in the values and structures of the quenching cross-sections, Figs. 6 and 7. None of the cross-sections studied show prominent resonance structure at low energies, making the averaging process (equation 5) for computing rates quite straightforward. Also, for $E_c \gtrsim 50\,\text{cm}^{-1} \sim E_{GM}$ (*cf.* Table 1), the cross-sections become smooth and exponentially decreasing.
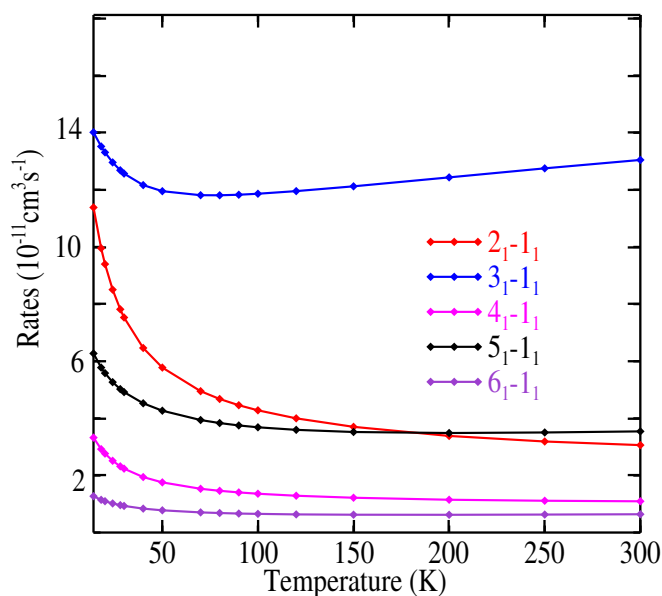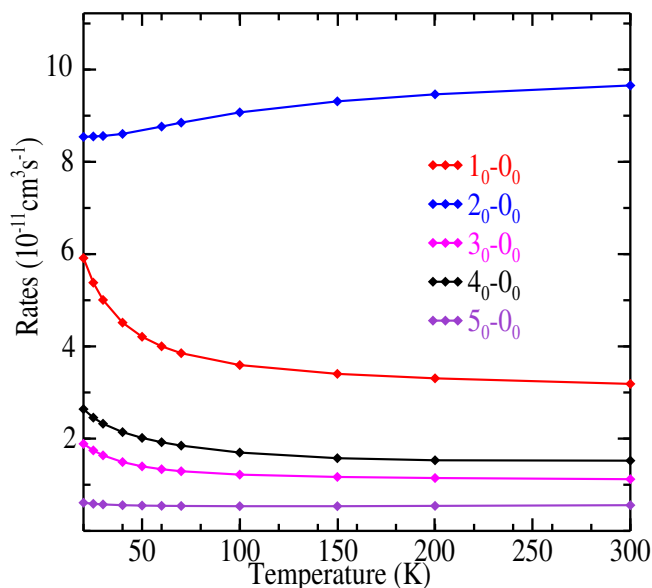
Fig. 9 Temperature dependence of rates for A-CH$_3$CN and E-CH$_3$CN in collision with He for transitions corresponding to the 220 GHz observation band. See Fig. 7 for cross-sections.

Fig. 8 Temperature dependence of rates for A- (top panel) and E- (bottom panel) CH$_3$CH in collision with He for transitions corresponding to the ground state. See Fig. 6 for cross-sections.
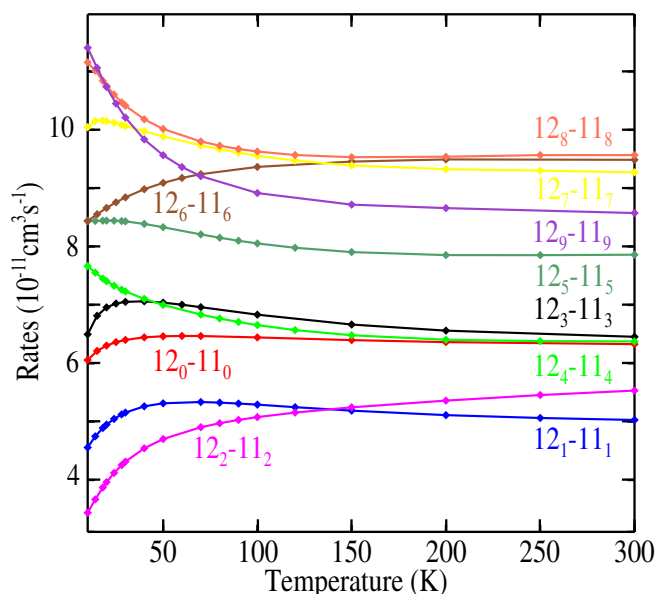
However, all cross-sections (and rates) have magnitudes that *do not* follow simple propensity rules, not for the magnitude of the change of angular momentum J, nor for the energy exchanged. For example, figures show that even quenching transitions $\Delta J = -2, -4$ dominate odd changes, $\Delta J = -1, -3$. This could reflect the rod-like structure of CH$_3$CN, with a similar role given to both ends of the rod irrespective of the dipole (see the same effect in collisions with the high-dipole, long rod of cyanoacetylene, HC$_3$N[38]). Rates follow the same rules. However, even if sections look very similar along a K ladder (the 220 GHz transitions, Figs. 7 and 9), the low-temperature end displays a very different order, pointing perhaps to difficulties in interpreting low-temperature observations.

Because of the great importance of the CH$_3$CN molecule and its extensive occurrence, rates of quenching of CH$_3$CN were computed some time ago by Green *et al.*[10] using a much simpler approach, both for the potential energy surface and for the dynamics. This early paper restrained all dynamics either to the CS approximation ($E_{tot} \leq 80\,\text{cm}^{-1}$), or to the IOS approach, whereby angular algebra is properly described, but the dynamics neglects all energy differences between the various rotational levels.

As we carry out here a computation using as precise a method as is possible, for all practical purposes, its is important to compare the present collision rates with those

made by Green in 1985,[10] taken from the LAMDA database (http://home.strw.leidenuniv.nl/moldata/)*.

This comparison is illustrated in Fig. 10 for both A- and E-CH_3CN···He. All quenching rates are computed at 100K. We see that the comparison is very different for optically allowed dipolar transitions (the red circles) and all others. While for those (in red), the CS/IOS computation of Green remains within a factor of 2 with respect to the present computations, all other quenching rates are very different, by factors of up to 1000. It is noticeable that the smaller the IOS rates, the larger the ratio between IOS and CC/CS dynamics. For larger, but optically forbidden rates, ratios from 1 to 100 are found. It must be also stressed that nearly all optically forbidden rates are larger now than those published in the databases. On the contrary, the optically allowed rates tend to decrease in CC/CS dynamics, albeit to a smaller extent. Because of these contradictory trends, it is very unclear what the effect of the new rates would have to actual observations, or more simply, to the validity of LTE approximation (Local Thermodynamical Equilibrium, $T_{kinetic} = T_{rotational}$), with such a large number of collisionally allowed, optically forbidden transitions, it is also unclear whether the notion of critical density retains a precise meaning.

We have computed a new 3D-PES for the interaction CH3CN–He in the rigid molecule approach by means of a CCSD(T)-F12b formalism. Using this PES, quenching rates of CH_3CN in collision with He have been computed. The resulting tables were put in the LAMDA format, for levels up to and $7K \leq T \leq 300K$, up to $J_K = 18_9$. They are available as supplementary material to this paper, and will be included in the various relevant databases.
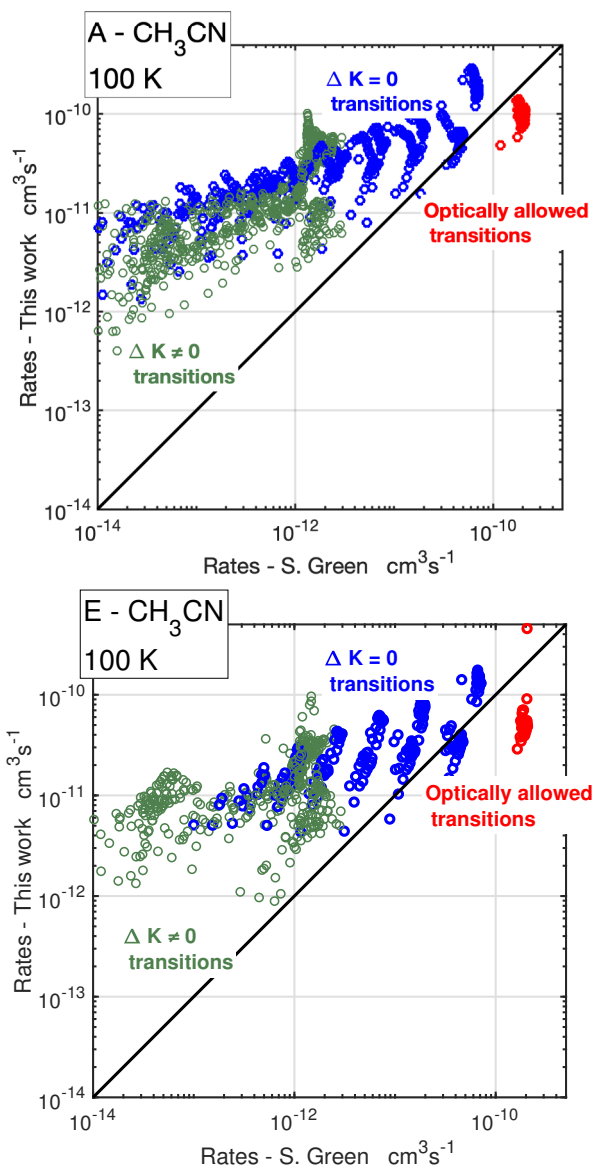
Acknowledgments

Fig. 10 Comparison of de-excitation rates between our work and the published LAMDA rates, from Green *et al.*, 1985. Black diagonal, equal rates. Red circles, dipolar transitions optically allowed ($\Delta J = -1$, $\Delta K = 0$). Blue circles, transitions within a same ladder, but with $\Delta J < -1$, , $\Delta K = 0$. Green circles, all quenching transitions ($\Delta J = 0, \pm 1, \pm 2, \ldots\ldots$) with $\Delta K = \pm 3, \pm 6, \ldots$ (*A* symmetry), or $\Delta K = \pm 1, \pm 2, \pm 4, \pm 5, \ldots$ (*E* symmetry).

---

* We are applying a scale factor coefficient which is equal to the square root of the reduced mass ratio collisions with H_2 *vs.* collisions with He. Note that the original Green computations were performed with He as a projectile.

Notes and references

1 D. Woon, *The Astrochymist*, http://www.astrochymist.org/.

2 P. M. Solomon, K. B. Jefferts, A. A. Penzias and R. W. Wilson, *Astrophys. J. Lett.*, 1971, **168**, L107.

3 S. Pols, A. Schwörer, P. Schilke, A. Schmiedeke, Á. Sánchez-Monge and T. Möller, *Astronomy & Astrophysics*, 2018, **614**, A123.

4 H. E. Matthews and T. J. Sears, *Astrophys. J. Lett.*, 1983, **267**, L53–L57.

5 S. Cazaux, A. G. G. M. Tielens, C. Ceccarelli, A. Castets, V. Wakelam, E. Caux, B. Parise and D. Teyssier, *Astrophys. J. Lett.*, 2003, **593**, L51–L55.

6 M. Agúndez, J. P. Fonfría, J. Cernicharo, J. R. Pardo and M. Guélin, *Astronomy & Astrophysics*, 2008, **479**, 493–501.

7 B. L. Ulich, *Nature*, 1974, **248**, 121–122.

8 K. I. Öberg, V. V. Guzmán, K. Furuya, C. Qi, Y. Aikawa, S. M. Andrews, R. Loomis and D. J. Wilner, *Nature*, 2015, **520**, 198–201.

9 L. Olmi, R. Cesaroni, R. Neri and C. Walmsley, *Astronomy and Astrophysics*, 1996, **315**, 565–577.

10 S. Green, *J. Phys. Chem.*, 1985, **89**, 5289–5294.

11 M. Le Guennec, G. Wlodarczak, J. Burie and J. Demaison, *Journal of Molecular Spectroscopy*, 1992, **154**, 305–323.

12 G. Knizia, T. B. Adler and H.-J. Werner, *J. Chem. Phys.*, 2009, **130**, 054104.

13 K. A. Peterson, T. B. Adler and H.-J. Werner, *J. Chem. Phys.*, 2008, **128**, 084102.

14 K. B. Gubbels, S. Y. v. d. Meerakker, G. C. Groenenboom, G. Meijer and A. v. d. Avoird, *The Journal of chemical physics*, 2012, **136**, 074301.

15 K. M. Walker, F. Dumouchel, F. Lique and R. Dawes, *The Journal of chemical physics*, 2016, **145**, 024314.

16 R. A. Kendall, T. H. Dunning Jr and R. J. Harrison, *The Journal of chemical physics*, 1992, **96**, 6796–6806.

17 F. Weigend and R. Ahlrichs, *Physical Chemistry Chemical Physics*, 2005, **7**, 3297–3305.

18 H.-J. Werner, P. J. Knowles, G. Knizia, F. R. Manby and M. Schütz, *Wiley Interdisciplinary Reviews: Computational Molecular Science*, 2012, **2**, 242–253.

19 E. Sahnoun, L. Wiesenfeld and K. Hammami, *The Journal of Physical Chemistry A*, 2020, **124**, 3242–3248.

20 M. Ben Khalifa, E. Sahnoun, L. Wiesenfeld, F. Khadri, K. Hammami, O. Dulieu, S. Spezzano and P. Caselli, *Physical Chemistry Chemical Physics (Incorporating Faraday Transactions)*, 2019, **21**, 1443–1453.

21 S. Sur, E. Quintas-Sánchez, S. A. Ndengué and R. Dawes, *Physical Chemistry Chemical Physics*, 2019, **21**, 9168–9180.

22 A. Faure, P. J. Dagdigian, C. Rist, R. Dawes, E. Quintas-Sánchez, F. Lique and M. Hochlaf, *ACS Earth and Space Chemistry*, 2019, **3**, 964–972.

23 S. Sur, S. A. Ndengue, E. Quintas-Sánchez, C. T. Bop, F. Lique and R. Dawes, *Physical Chemistry Chemical Physics*, 2020.

24 C. T. Bop, F. A. Batista-Romero, A. Faure, E. Quintas-Sánchez, R. Dawes and F. Lique, *ACS Earth and Space Chemistry*, 2019, **3**, 1151–1157.

25 B. Desrousseaux, E. Quintas-Sánchez, R. Dawes and F. Lique, *The Journal of Physical Chemistry A*, 2019, **123**, 9637–9643.

26 E. Quintas-Sánchez and R. Dawes, *Journal of Chemical Information and Modeling*, 2019, **59**, 262–271.

27 R. Dawes and E. Quintas-Sánchez, *Reviews in Computational Chemistry vol. 31*, 2018, ch. 5, pp. 199–264.

28 J. M. Hutson and S. Green, *MOLSCAT computer code, version 14, Distributed by Collaborative Computational Project 6*, Warington, UK: Daresbury Laboratory, 1995.

29 H. S. P. Müller, B. J. Drouin, J. C. Pearson, M. H. Ordu, N. Wehres and F. Lewen, *Astronomy & Astrophysics*, 2016, **586**, A17.

30 A. M. Arthurs and A. Dalgarno, *Proceedings of the Royal Society of London Series A*, 1960, **256**, 540–551.

31 P. McGuire and D. J. Kouri, *Journal of Chemical Physics*, 1974, **60**, 2488–2499.

32 A. Faure, P. Valiron, M. Wernli, L. Wiesenfeld, C. Rist, J. Noga and J. Tennyson, *J. Chem. Phys.*, 2005, **122**, 221102–221102.

33 T. Stoecklin, O. Denis-Alpizar, A. Clergerie, P. Halvick, A. Faure and Y. Scribano, *The Journal of Physical Chemistry A*, 2019, **123**, 5704–5712.

34 T. Stoecklin, O. Denis-Alpizar, P. Halvick and M.-L. Dubernet, *The Journal of chemical physics*, 2013, **139**, 034304.

35 A. Faure, L. Wiesenfeld, M. Wernli and P. Valiron, *J. Chem. Phys.*, 2005, **123**, 104309–104309.

36 M. D. Wheeler and A. M. Ellis, *Chemical Physics Letters*, 2003, **374**, 392–399.

37 N. Troscompt, A. Faure, L. Wiesenfeld, C. Ceccarelli and P. Valiron, *Astron. Astroph.*, 2009, **493**, 687–696.

38 A. Faure, F. Lique and L. Wiesenfeld, *Mon. Not. Royal Astron. Soc.*, 2016, **460**, 2103–2109.